The Journal of Supercritical Fluids 220 (2025) 106546

Contents lists available at ScienceDirect

The Journal of Supercritical Fluids

journal homepage: www.elsevier.com/locate/supflu

Measurement of phase transition, density and viscosity of supercritical carbon dioxide-Fischer-Tropsch wax mixtures

Andri Swanepoel [a,b], Philip W. Labuschagne [b], Cara E. Schwarz [a,*]

[a] Department of Chemical Engineering, Stellenbosch University, Banghoekweg, Stellenbosch 7600, South Africa
[b] Centre for Nanostructures and Advanced Materials, Council for Scientific and Industrial Research, Meiring Naude Road, Pretoria 0001, South Africa

HIGHLIGHTS

- Non-functionalised waxes undergo melting temperature increases in CO_2.
- Oxidised wax undergoes a slight depression in melting temperature.
- Pressure induced recrystallisation of lower M_W FT wax.
- The lowest M_W FT wax displays a temperature inversion.
- Solubility is accurately predicted with the modified Chrastil model.

GRAPHICAL ABSTRACT

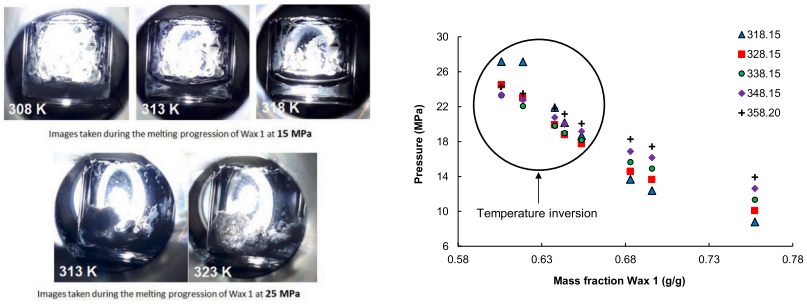

ARTICLE INFO

Keywords:
Carbon dioxide
Wax
Phase transition
Density
Viscosity

ABSTRACT

Melting temperature, phase behaviour and densities of binary mixtures of CO_2 and three Fischer-Tropsch waxes with varying molecular weights were experimentally determined. The melting temperatures of the lower molecular weight waxes increased with CO_2 pressure, and pressure induced crystallisation of the lowest molecular weight wax occurred above 20 MPa. CO_2 solubility in the waxes decreased with increasing wax molecular weight. Trends in mixture densities with changes in temperature and pressure mimicked that of pure CO_2. The viscosity of the lowest molecular weight wax decreased with increased CO_2 concentration, and decreased with increases in temperature and pressure, with the impact of pressure minimised above the temperature inversion point. Solubility data were correlated with a modified Chrastil and the Mendez-Santiago & Teja models. The Chrastil model accurately predicted solubility of CO_2 in all three waxes to within 1 % of the measured values.

1. Introduction

Synthetic wax particles are utilised in a wide variety of applications, including coatings, inks, paint and personal care products. The size (distribution) and morphology of the particles are critical in ensuring that the final product conforms to its intended quality and efficacy requirements. Popular conventional particle/powder production technologies such as milling, crushing, grinding, sublimation, crystallisation and spray drying require the application of mechanical force, high temperatures, high water consumption and/or the use of organic solvents, all undesirable from an energy cost saving and health/environmental standpoint [1,2].

* Corresponding author.
E-mail address: cschwarz@sun.ac.za (C.E. Schwarz).

https://doi.org/10.1016/j.supflu.2025.106546
Received 28 November 2024; Received in revised form 7 February 2025; Accepted 7 February 2025
Available online 10 February 2025

Table 1
Waxes and chemicals used in this study.

Wax	M_w (g/mol)	T_m (K) (peak)*	T_m (K) (complete)**	Supplier
Wax 1 (product code: CB505)	457.5	313.2	317.8	Cirebelle (ZA)
Wax 2 (product code: CB303)	546.1	332	363.8	Cirebelle (ZA)
Wax 3 (oxidised) (Product Name: Sasolwax A28)	895	372.7	375.2	Sasol (ZA)
Chemical	**CAS number**	**Purity (w/w)**	**Product Number**	**Supplier**
Carbon Dioxide	124–38–9	0.9999	K243C	Air Products (ZA)
Glycerol Monostearate		0.995	76967–0104	Croda Chemicals (ZA)
n-Dodecane	112–40–3	> 0.99	D221104–2.5 L	Sigma-Aldrich (ZA)

* Peak T_m refers to maximum of the DSC main melting peak as shown in Fig. 4
** Complete T_m refers to the temperature where complete melting of the wax was observed in the fixed volume static view cell at atmospheric pressure

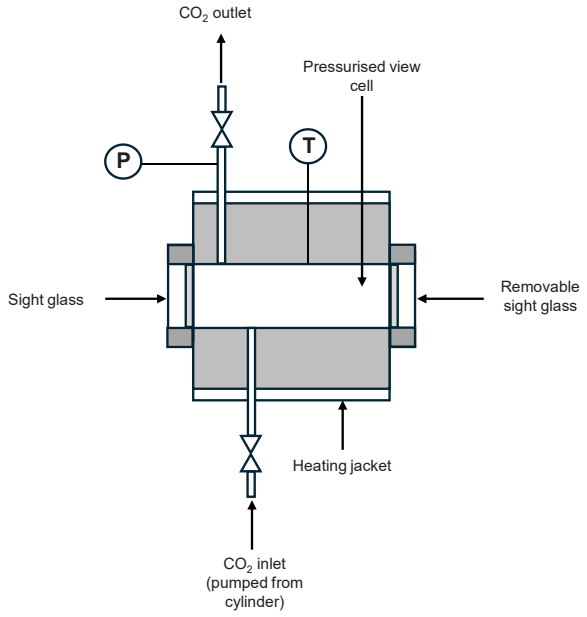

Fig. 1. Schematic of the static high pressure view cell utilised to determine the T_m under supercritical conditions of the three synthetic waxes.

The Particles from Gas Saturated Solutions (PGSS) process, first patented by Weidner et al. [3] uses supercritical carbon dioxide (sc-CO_2) as plasticiser for the micronisation of compatible compounds under facile conditions, without the need for water, organic co-solvents and in an oxygen free environment [4,5]. The simple process can produce powder in the micron size range with inherent process flexibility via tuning of process parameters (e.g. temperature, pressure etc.).

Solid-liquid-gas (S-L-G) equilibria of CO_2 and various compounds have been shown to be highly informative in predicting the outcomes of micronisation and crystallisation using different supercritical CO_2 processing methods [1,2]. For the PGSS process specifically, knowledge of the influence of CO_2 on the melting temperature (T_m) of the heavy compound and knowledge of the degree of solubility of CO_2 in the molten compound are critical parameters required for process optimisation [1,6].

Two competing effects can be observed when a compressed gas is dissolved in a molten heavy compound, namely an increase in T_m as a result of increasing hydrostatic pressure, as well as a reduction in T_m of the heavy compound as a result of the presence of the dissolved gas [7]. Interaction between CO_2 and functional groups within the heavy compound causes disruption of the intermolecular interactions of the heavy compound and in the case of polymers, leads to increased polymer chain mobility and distance between polymer chains [8], resulting in reduced T_m. The interactions between CO_2 and functional groups are as a result of weak Lewis acid-base interactions between the acidic CO_2 and electron-donating functional groups within the heavy compound/polymer [9].

The influence of processing conditions on the viscosity of the molten compound is also an important factor in the ease of processability of materials for micronisation via PGSS [10,11]. The viscosity of compounds exposed to sc-CO_2 is closely linked to density of the CO_2 at the specific temperature and pressure conditions as the density of CO_2 influences the degree to which the CO_2 can dissolve in the compound(s) to be processed. Detailed knowledge of the phase behaviour and influence of pressure and temperature thereon is thus extremely valuable to accurately guide the process conditions to be used during micronisation.

Fischer-Tropsch (FT) waxes are versatile synthetic hydrocarbon waxes produced from a gas to liquids process. Literature is available on the measurement and modelling of the phase behaviour of comparable compounds such as long chain *n*-alkanes dissolved in sc-CO_2, including carbon numbers C24 [12–15], C25 [12,13,15], C28 [12–14,16,17], C29 [12,13,15], C30 [17], C32 [12], C33 [12] and C36 [12,14], as well as for solubility of CO_2 in polyethylene [18–21] and polypropylene [18, 22–26]. Limited literature is however available on the behaviour of sc-CO_2 dissolved in long chain *n*-alkanes [14]. Fractionation of paraffin wax with sc-CO_2 has been performed [27], as well as supercritical micronisation of synthetic waxes, albeit with the Rapid Expansion from Saturated Solutions (RESS) process, in sc-CO_2 [28] and in supercritical propane [29]. There is however a lack of information on the phase behaviour, density and viscosity of binary mixtures of sc-CO_2 and FT waxes, thus motivating this work.

The aim of this work was to measure phase behaviour and physical properties of sc-CO_2 and three FT waxes with different ambient T_m, in order to inform on the range of processing conditions that can be utilised for PGSS micronisation of the waxes. The phase equilibria and density of all three systems were successfully measured, while the viscosity of mixtures of the lowest melting point wax and sc-CO_2 could also be measured.

2. Experimental

2.1. Materials

The product information of the waxes and chemicals used in this study is shown in Table 1. The FT waxes and their weight average molecular weights were kindly provided by Cirebelle (South Africa) and Sasol (South Africa). All chemicals were used without any further purification.

2.2. Methodology

2.2.1. Melting point behaviour

Thermal analyses of the wax materials were performed using a differential scanning calorimeter (DSC Q2000, TA Instruments, New Castle, Delaware, USA). Samples of between 0.5 mg and 2 mg were prepared in aluminium sample pans and analysed in a nitrogen atmosphere maintained at a flow rate of 10 mL/minutes. Heating and cooling were performed at 10 K/minutes between 243 K and 473 K. For all samples the results from the first heating cycle are given to provide a representative image of the conditions under which melting took place. The DSC results provide information on the melting behaviour at atmospheric pressure.

A static high-pressure view cell with an internal volume of 25 cm^3

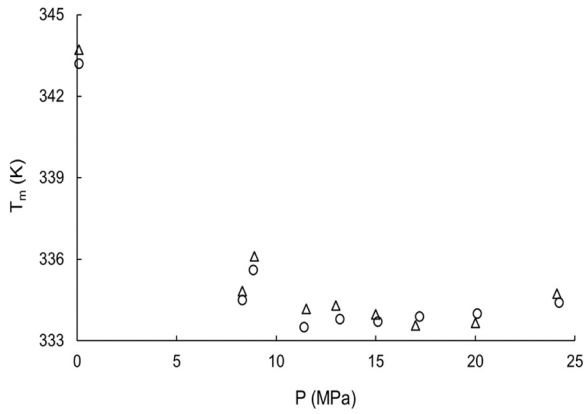

Fig. 2. Comparison of T_m of glycerol monostearate + CO_2 measured with the static fixed volume view cell to data from [30], (Key, Δ = measured data and ○ = data from [30]).

(Top Industrie, Vaux-le-Pénil, Île-de-France, France) was utilised to determine the impact of sc-CO_2 on the melting behaviour of the waxes as compared to atmospheric pressure (shown in Fig. 1). Approximately 50 mg of wax was loaded into a small glass vial and allowed to equilibrate to the set temperature. The view cell was pressurised to a set pressure using a membrane pump (Milton Roy, USA), with pressure in the view cell regulated via a back pressure valve. The temperature was gradually increased in increments of 0.1 K every 5 minutes. The melting progression was visually determined, with T_m recorded as the point of complete melting of the sample. Triplicate experiments were performed at each chosen pressure setting. Pressure was measured with an Ashcroft (USA) pressure sensor and temperature was measured with a 3-wire PT 100 probe (Top Industrie, France).

The method was validated by measuring the T_m of glycerol monostearate (GMS) and comparing the results to data from literature [30], with the measured values comparing well to that of the published data, as shown in Fig. 2.

2.2.2. Phase behaviour and thermophysical properties

The experimental setup and procedures used for the concurrent measurement of phase transition, density and dynamic viscosity were described in detail previously [31–33]. An abbreviated description of the equipment and experimental procedures is given below.

2.2.2.1. Phase boundary. A synthetic visual method was used to determine phase equilibria of binary mixtures of the three waxes and sc-CO_2. Two different high-pressure variable volume view cells that had previously been verified were used to measure the data, for Wax 1 [31], and for Wax 2 and Wax 3 [34]. A similar procedure was used in both cells. A known mass of wax was added to the cell. The cell was sealed and cleared of any air using a vacuum pump and flushed with CO_2. A known mass of CO_2 was added to the cell, and the cell was heated to the desired temperature, pressurised and allowed to equilibrate while the mixture was stirred with a magnetic stirrer bar and plate. The pressure in the cell was then gradually and isothermally reduced until a phase transition was observed. Visual observations were performed via a HD camera fitted to the sight glass of the cell. Approaching the phase transition from the one phase region and with a sufficiently slow pressure decrease ensured the mixture was not supersaturated and thus accurate measurements were taken.

The phase transition pressure was noted and the procedure repeated until the transition pressure could be measured in a reproduceable manner to within 0.02 MPa. The temperature of the cell was further increased to the next desired point of measurement and the process was repeated. Pressure was measured with a ONEhalf20 (USA) melt pressure transducer (Wax 1) and an Industrial Sensors Inc (USA) pressure transducer (Wax 2 and Wax 3), and temperature with a 3-wire PT 100 probe (WIKA Instruments, ZA) (Wax 1), and a 4-wire PT100 probe (WIKA Instruments, ZA) (Wax 2 and Wax 3). Phase transition pressures were measured up to 30 MPa in accordance with the operational limits of the equipment as well as internal safety requirements.

2.2.2.2. Density. Density of high-pressure systems can be measured via magnetic suspension balances [11,19,22,24,35], or by using a vibrating wire [36,37] or vibrating tube [35,38,39]. In this work the density of a mixture at the phase transition was calculated from the known mass and composition of the mixture in the variable volume view cell close to the phase boundary data in combination with the calibrated volume of the cell [32–34]. This simple yet accurate method allows for calculation of the density at the same composition and nearly identical temperature and pressure as the phase transition. Calibration was performed by loading a known mass of pure CO_2 to the cell, followed by heating and pressurisation of the cell. The piston position was systematically varied and at each position the displacement, temperature and pressure were noted. The piston displacement was measured via an Insize 300 mm digital gauge (model: 1150–300) to within 0.01 mm. The density of CO_2 at each of the recorded temperature and pressure points was calculated using the Equation of State of Span and Wagner [40]. The cell volume as related to a specific piston position was then calculated using these densities and the known mass of CO_2 loaded to the cell.

This volume-piston position correlation was subsequently utilised to determine the density of the mixture of known mass and composition loaded to the cell at the piston position corresponding to phase transition temperature and pressure. These measurements were performed in the single phase region. Temperature and pressure were measured with the same equipment used for determination of the phase boundaries.

2.2.2.3. Dynamic viscosity. The converse piezoelectric effect was utilised to measure dynamic viscosity of mixtures of CO_2 + Wax 1. Due to the limitations of the equipment and the viscous nature of Wax 2 and Wax 3, the viscosities for mixtures of Wax 2 and Wax 3 with CO_2 could not be measured.

A torsional quartz crystal previously described [31] was inserted into the cell before loading of a mixture. An electrical signal with a known frequency was then passed through the crystal, causing the crystal to vibrate at the same frequency as the incoming electrical signal. When immersed in a mixture, the propagation of these vibrations is damped by the surrounding mixture. The difference between the resonance of the crystal in a vacuum (i.e. where no damping occurs) and that of the crystal in a mixture when excited by an electrical signal of the same frequency can be directly related to dynamic viscosity of the mixture [41], as expressed in Eq. 1.

$$f_0 - f_{res} = k \cdot \sqrt{f_{res} \cdot \pi \cdot \eta \cdot \rho_f} \quad (1)$$

In this equation f_0 (Hz) is the resonance of the crystal under vacuum, f_{res} (Hz) is the crystal's resonance when immersed in a fluid, k (m^2/kg) is the electromechanical constant of the crystal, η is the fluid viscosity (mPa.s), and ρ_f (kg/m^3) is the density of the fluid.

The vacuum resonance of the crystal was measured at a range of temperatures used in this work to account for the temperature dependence of the electromechanical constant [31]. The electrical signals that were passed through the crystal were generated by a Picoscope 2206B oscilloscope. From this data a linear relationship was determined between the vacuum resonance and temperature so that small variations in temperature between experiments could be accurately accounted for in the value of f_0 used to determine viscosity.

The resonance frequency of *n*-dodecane was measured at the experimental temperatures and between 0.1 MPa and 30 MPa. Known values of density and viscosity of *n*-dodecane (from the National Institute of Standards and Technology (NIST)) were then used to determine the values for *k* at these experimental conditions. A ten times

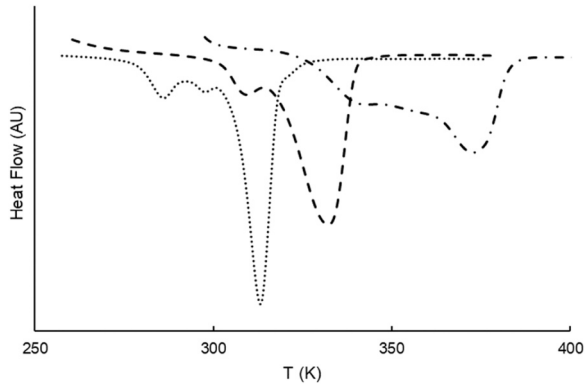

Fig. 3. DSC melting curves of the three waxes under investigation, from left to right: Wax 1 (dotted line), Wax 2 (dashed line) and Wax 3 (dash dot line).

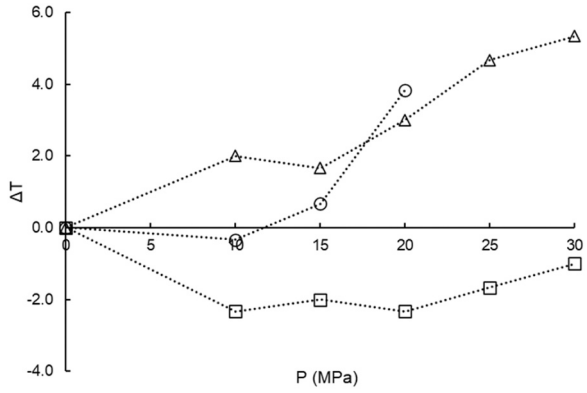

Fig. 4. Changes in complete melting temperature for the three waxes with pressure, with T (complete melting) at P_0 for Wax 1 = 317.8 K, Wax 2 = 363.8 K and Wax 3 = 375.2 K (Key: ○ = Wax 1, Δ = Wax 2 and □ = Wax 3).

compensation was applied to the oscilloscope probes used to measure the resonant frequencies to improve the accuracy of the viscosity measurements [33]. The pressure dependency of k was adjusted for by the application of a linear correlation relating k to the experimental pressure (see Eq. 2), as applied previously [33].

$$k = A + BP \tag{2}$$

The values for A and B were determined by fitting Eq. 1 to the known values of density and viscosity obtained from NIST along with the experimentally measured pressures and resonance frequencies in *n*-dodecane.

Viscosity of the CO_2 + wax mixtures were determined by measuring f_{res} of a mixture at the experimental temperatures and pressures 0.2 MPa to 0.8 MPa above the previously observed phase transition pressures. The resonance frequency was measured by passing an electrical current through the crystal immersed in the mixture, and the subsequent voltage output was plotted to determine the frequency where the minimum voltage loss occurred. This frequency was taken as f_{res} and, in combination with the mixture density, used to determine viscosity via Eq. 1.

2.2.2.4. Uncertainty. The uncertainties pertaining to the experimental data are primarily Type B standard uncertainties as indicated by the "Guide to the expression of uncertainty in measurement" [42]. Uncertainty of the temperature measurements was calculated based on the calibration of the temperature probe as well as observed fluctuations in temperature readings, and equalled 0.3 K for the fixed volume cell and 0.14 K for the variable volume cells. The combined standard uncertainty in pressure measurements was calculated as 0.05 MPa for the static cell and 0.06 MPa for the variable volume view cells. These uncertainties include not only the uncertainty at which the phase transition is measured but also the accuracy and reproducibility of the sensors. The uncertainty in the compositions of the mixtures measured were based on the accuracy of the weighing and loading of the CO_2 and the waxes, calculated as 0.12 g and 0.044 g respectively. The combined standard uncertainty in the compositions reported was subsequently determined to be 0.0034 g/g. Combined standard uncertainty in density measurements (based on the uncertainties of weighing and loading the CO_2 and waxes, as well as the uncertainty in the volume calibration of the cells) was calculated as u (ρ) < 0.13.ρ kg/m^3. The standard uncertainty in viscosity measurements was determined as a combination of the uncertainties in temperature, pressure, composition and the equipment, and was calculated as u (η) < 0.153.η mPa.s.

3. Results

3.1. Melting behaviour

The DSC melting profiles (first heating cycle) of the three waxes under ambient pressure are shown in Fig. 3.

Wax 1 displays two distinct small peaks at 286.1 K and 298.6 K before a main peak with an average melting point of 313.2 K. Wax 2 displays a broader main melting peak, with a single peak at 309.2 K to the left of the main melting peak, with a $T_{m(avg)}$ of 332.0 K. Wax 3 shows a broad irregular melting peak with a maxima at 372.7 K. The multiple melting peaks visible for Wax 1 and Wax 2 below the average melting temperatures are indicative of solid-solid transitions between orthorhombic and hexagonal crystal forms due to the presence of so-called "rotator" phases [43,44]. Waxes that melt below 333 K generally exhibit two solid-solid phase transitions between the orthorhombic and hexagonal states, while those melting between 333 K and 348 K display only one solid-solid transition [45]. As the chain lengths increase for higher melting point waxes (with carbon number greater than 39, or melting above 348 K), chain mobility is hindered, and the solid state orthorhombic-hexagonal transition is no longer possible [46].

The impact of supercritical conditions on the melting temperature of the three waxes was determined via the use of a high-pressure fixed volume static view cell. The changes observed in the complete melting temperature with pressure (with ΔT equal to the observed complete T_m under supercritical conditions minus T_m at ambient pressure (P_0)) for the three waxes are shown in Fig. 4.

For both Wax 1 and Wax 2 a slight increase in the complete T_m is observed with an increase in pressure as compared to the complete T_m measured in the view cell under atmospheric pressure. This can be attributed to hydrostatic pressure dominating the melting behaviour in the absence of functional groups to interact with sc-CO_2. In the case of the oxidised wax, a slight melting temperature depression is observed as a result of interaction of the sc-CO_2 with the carbonyl groups added to the wax during the oxidation process. As the pressure is increased to 30 MPa, the T_m of Wax 3 increases again, due to the increasing influence of hydrostatic pressure on the melting behaviour. This behaviour has been observed in GMS [30], as well as stearic acid, palmitic acid and myristic acid [47].

The melting temperatures of Pluronic block co-polymers [48], high molecular weight polyethylene glycols (PEGs) [49] as well as natural compounds such as shellac [50] showed decreases in melting temperatures under sc-CO_2 up until a certain pressure, after which the melting temperature remained constant. It is postulated that the longer chains and more complicated structures (consisting of a greater number of side chains and denser chain folding) of these compounds counteract the hydrostatic pressure that affects the melting temperatures of smaller molecules at pressures well above the critical point. In this regard Wax 3 thus behaves more like the shorter chain fatty acids than the higher molecular weight Pluronics or high molecular weight PEGs.

In the case of Wax 1, a complete melting temperature could not be

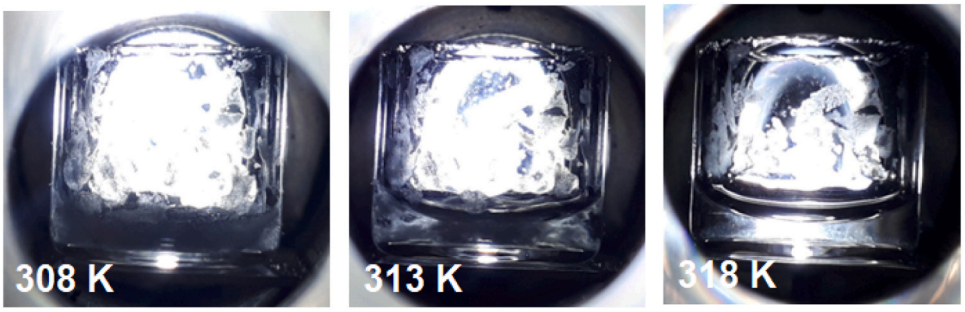

Fig. 5. Melting progression of Wax 1 under supercritical CO_2 conditions at 15 MPa and at 25 MPa.

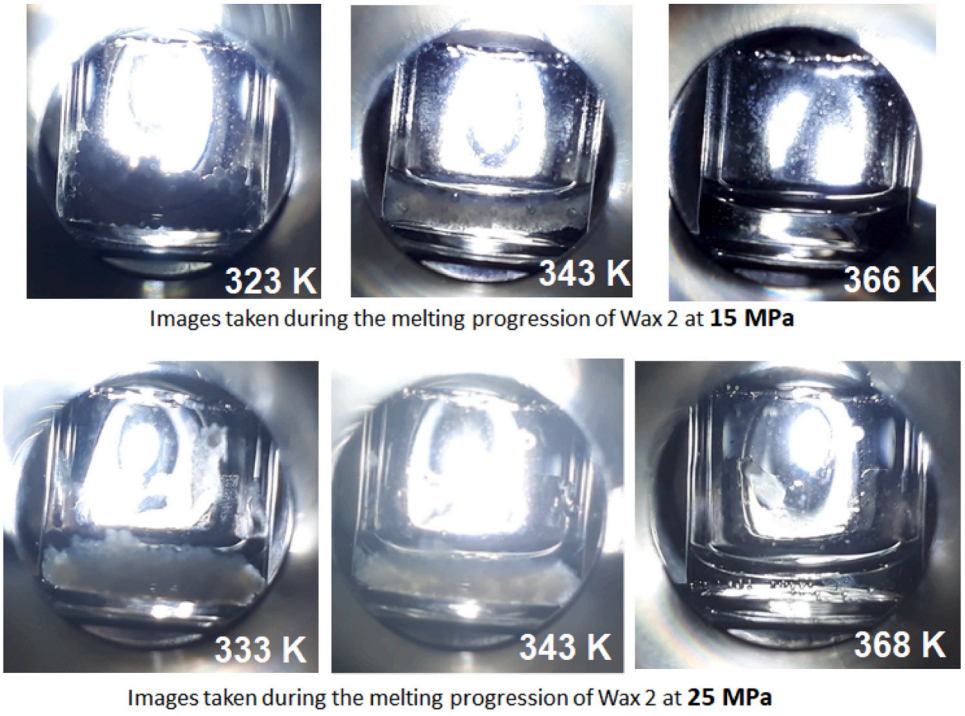

Fig. 6. Melting progression of Wax 2 under supercritical CO_2 conditions at 15 MPa and 25 MPa.

visually determined above 20 MPa. At higher pressure, as the temperature is increased, what appears to be solid wax is formed in the vial that remains even as the temperature is increased further, instead of a clear liquid, as seen in Fig. 5. In comparison, Wax 2 (Fig. 6) and Wax 3 remained molten as pressure increased until the final melting temperature was identified (indicated by a clear liquid).

When studying the DSC thermograms of the three waxes, it is observed that Wax 1 has the narrowest main melting peak, followed by Wax 2. It was shown that for ultra-high molecular weight polyethylene, there exists a correlation between melting peak broadness and entanglement density [51]. At greater entanglement density, chain extension is hindered and reduces lamellar thickening - resulting in broader

Table 2
Experimental phase behaviour data (temperature (T) and pressure (P)) for CO_2 + Wax 1 at various wax concentrations (X_{wax}), as well as density (ρ) and dynamic viscosity (η) measured at the phase transition.

X_{wax} [g/g]	T [K]	P [MPa]	ρ (kg/m^3)	η (mPa.s)	Pressure-Temperature relationship, $P = AT^3 + BT^2 + CT + D$ with P in MPa and T in K					Density - Temperature relationship, $\rho = AT^2 + BT + C$ with ρ in kg/m^3 and T in K			
					A	B	C	D	R	A	B	C	R
0.606	319.1	26.8	843.3	1.000	−5.0714E−05	0.0575	−21.5652	2697.64	0.999		−1.4598	1307.51	0.995
	328.1	24.5	828.1	0.737									
	338.3	23.2	811.5	0.614									
	348.8	23.4	797.5	0.521									
	358.3	24.3	786.2	Not measured									
0.619	317.7	27.5	838.4	0.902	−2.7399E−04	0.2861	−99.4866	11542.4	0.997	1.2868E−02	−10.1201	2754.10	0.999
	327.8	22.9	818.2	0.738									
	337.8	22.2	804.2	0.636									
	347.8	22.6	791.8	0.567									
	358.1	23.5	779.8	Not measured									
0.638	318.0	22.0	829.6	0.925	−1.5771E−04	0.165	−57.452	6674.42	0.995	8.6266E−03	−7.1254	2222.75	0.999
	327.6	19.9	813.6	0.781									
	337.8	19.9	800.4	0.692									
	347.5	20.6	788.7	0.607									
	358.4	21.8	776.9	Not measured									
0.644	317.7	20.3	Not measured	0.888	−1.2827E−04	0.1344	−46.7986	5438.85	0.997		−1.3360	1288.48	0.995
	327.8	18.7		0.727									
	337.9	19.0		0.624									
	348.0	19.9		0.541									
	358.9	21.2		Not Measured									
0.654	317.9	18.7	827.6	1.093	−1.2411E−04	0.1289	−44.5336	5133.97	0.995		−1.3211	1246.85	0.999
	327.8	17.7	812.7	0.914									
	338.2	18.2	800.2	0.814									
	347.7	19.1	787.7	0.740									
	358.2	20.1	773.7	Not measured									
0.683	317.9	13.7	814.5	1.044		0.0008	−0.4363	70.01	0.998		−1.0917	1161.30	1.000
	327.8	14.4	803.2	0.875									
	338.0	15.7	792.6	0.755									
	348.2	16.9	780.7	0.636									
	357.9	18.2	770.9	Not measured									
0.696	317.6	12.5	816.4	Not Measured			0.1262	−27.78	0.996		−1.0642	1153.82	0.998
	327.8	13.4	804.8										
	337.9	14.8	793.9										
	348.1	16.1	782.5	0.862									
	358.2	17.5	773.5	Not measured									
0.757	317.9	8.7	799.3	1.288			0.1279	−31.90	1.000		−0.9015	1086.06	0.999
	327.8	10.0	790.3	1.074									
	338.2	11.4	782.0	0.924									
	348.5	12.7	771.8	0.804									
	358.3	13.8	762.8	Not measured									

melting peaks. At lower entanglement density sharper melting peaks are observed due to enhanced lamellar thickening. It can therefore be argued that as a result of this lower degree of entanglement, pressure induced crystallisation can occur more easily.

It has been proposed that the structure of a FT wax consists of four domains, including an amorphous phase, a rigid amorphous zone, a mobile amorphous oil phase and a crystalline phase that resembles the structure of a pure *n*-alkane [52,53]. The percentages of the total wax content that each of these zones represents vary depending on the hardness of the wax. Studies on the melting behaviour of FT waxes [52, 54–56] have shown that upon melting, motion occurs in the amorphous and crystalline regions, chain-end defect reorientations in the amorphous zone and translational re-orientational motion in the crystalline region. As the temperature increases, the solid amorphous zone becomes mobile leading to the formation of the mobile amorphous zone, and the transformation from solid to mobile amorphous phase is complete before the orthorhombic to hexagonal phase transition occurs [57]. Meanwhile, shorter chains in the crystallite phase also start to melt, while the longer chains remain solid. The melted chains migrate to and become immersed in the mobile amorphous zone, thus becoming part of the amorphous phase. When the hexagonal transition is reached, the crystalline chains will experience rapid rotation around their long axes leading to the weakening of the intermolecular Van der Waals forces. As evident from Fig. 3, Wax 1 undergoes two solid-solid transitions before melting commences, versus the single solid-solid transition of Wax 2. Wax 3 will not undergo any solid-solid transition as chain movement is hindered by longer chain lengths and a seemingly broad chain length distribution. Wax 1 will thus experience more chain movement and weakening of intermolecular Van der Waals forces as the temperature is increased.

This process is repeated as the temperature increases further, with the average chain length of the crystalline phase increasing and the solid

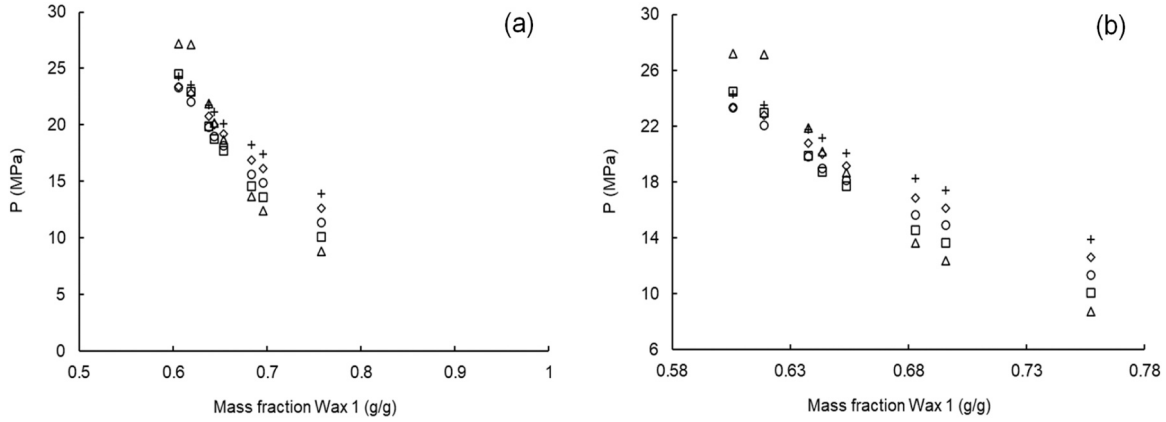

Fig. 7. Pressure-composition data for Wax 1 + CO_2 (a) between 0 MPa and 30 MPa and a wax mass fraction of 0.5–1 and (b) between 6 MPa and 30 MPa and a wax mass fraction of 0.58 and 0.78 (Key: Δ = 318.15 K, □ = 328.15 K, ○ = 338.15 K, ◊ = 348.15 K and + = 358.20 K.

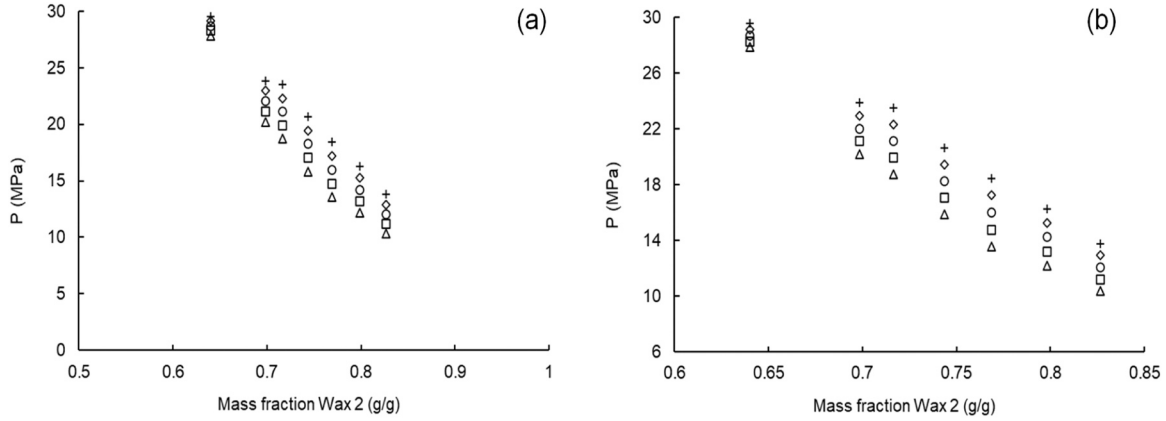

Fig. 8. Pressure composition data for Wax 2 + CO_2 (a) between 0 MPa and 30 MPa and a wax mass fraction of 0.5–1 and (b) between 6 MPa and 30 MPa and a wax mass fraction of 0.6 and 0.85 (Key: Δ = 358.20 K, □ = 368.20 K, ○ = 378.20 K, ◊ = 388.20 K and + = 398.20 K).

phase approached that of a pure *n*-alkane. Once the mobile amorphous zone has grown to a specific size, the remaining crystalline fraction becomes immersed in the amorphous zone. This corresponds to the apparent melting temperature. Once all these crystallites have melted completely and joined the mobile amorphous phase, complete melting is achieved.

It is postulated that due to greater chain mobility and a larger amorphous/oil content, upon heating Wax 1 is effectively fractionated into an amorphous component, containing shorter crystalline chains and chain defects, and a crystalline component. If this mobile zone becomes entrained in the sc-CO_2, the chain length distribution of the remaining crystalline fraction becomes progressively narrower with increasing temperature. This results in an effective increase in the average chain length of the crystalline fraction, and is possibly indicated by the sharp increase in melting temperature for Wax 1 between 15 MPa and 20 MPa in Fig. 4. As a result of the narrowing of the crystalline chain length distribution, above a certain pressure threshold, pressure induced crystallisation of this remaining crystalline fraction occurs, as evidenced by the fixed volume static view cell results.

Wax 2 displays only one solid-solid transition, at a much higher temperature than Wax 1, a higher average melting temperature and thus also a greater crystalline content. The slightly broader and much broader melting peaks of Wax 2 and Wax 3, respectively, also indicate that both waxes have broader chain length distributions than Wax 1, as is expected for Wax 3 as a result of the oxidisation process. It has also been shown that some high molecular weight FT waxes have bridged lamellae due to the presence of some very long chains, a so-called nematocrystalline chain packing [58,59], that will inhibit chain mobility.

Thus, as the melting temperature of a wax increases, its structure results in reduced chain mobility. As a result, the conditions for the creation of a crystalline phase in sc-CO_2 become less favourable.

3.2. CO_2 solubility / bubble point pressure

Phase equilibrium of CO_2 + wax mixtures of high wax fraction were analysed that are relevant to PGSS micronisation. As mentioned in the experimental section, a mixture of CO_2 and wax was loaded into the phase equilibria cell, and the bubble point pressures visually observed at five different temperature points, 10 K apart. This procedure was then repeated for the other binary mixtures with different compositions at the same temperature set points. To accurately compare the isothermal phase behaviour of the different mixtures measured on separate occasions, an expression correlating pressure as a function of temperature was generated for each mixture composition, as previously utilised [33,60]. The order of this expression was determined by applying linear regression to the pressure – temperature (PT) data for each mixture composition point. If the R^2 value of the linear regression at least equalled 0.99, a linear relationship between temperature and pressure was confirmed. If the R^2 value was found to be less than 0.99, a polynomial expression of increasing order was fitted to the data until an R^2 value of 0.99 or more could be obtained. While this approach was successful for Wax 1 + CO_2, the R^2 values of the P-T relationships for both Wax 2 and Wax 3 for all mixtures could only be fitted to $R^2 > 0.96$ but

Table 3
Experimental phase behaviour data (temperature (T) and pressure (P)) for system CO_2 + Wax 2 at various wax concentrations (X_{wax}), as well as density (ρ) measured at the phase transition.

X_{wax} [g/g]	T [K]	P [MPa]	ρ (kg/m^3)	Pressure-Temperature relationship, P = AT+B with P in MPa and T in K			Density - Temperature relationship, ρ = AT^2 + BT + C with ρ in kg/m^3 and T in K			
				A	B	R	A	B	C	R
0.640	360.9	27.9	808.9	0.04201	12.8129	0.965		−1.0067	1172.2878	0.998
	367.9	28.2	801.5							
	377.8	28.8	792.2							
	387.4	29.2	783.3							
	398.8	29.4	770.1							
0.698	357.8	20.0	796.8	0.09121	−12.4596	0.972		−0.9115	1122.7986	0.978
	369.2	21.3	786.8							
	376.5	22.1	780.7							
	389.1	22.6	764.3							
	400.8	24.2	759.7							
0.716	360.1	18.8	784.1	0.11905	−23.9136	0.998		−0.6081	1003.2735	0.997
	366.8	19.8	780.0							
	378.6	21.2	773.5							
	387.3	22.2	768.3							
	398.4	23.4	760.5							
0.744	358.3	15.7	791.5	0.12003	−27.1481	0.996	−0.0052	3.4944	205.6254	0.999
	368.5	17.1	788.3							
	378.2	18.4	785.3							
	388.7	19.6	779.8							
	398.8	20.6	773.9							
0.769	361.0	14.0	760.4	0.12302	−30.5193	0.997		−0.2201	838.8054	0.928
	371.3	15.1	755.6							
	381.6	16.2	751.6							
	388.0	17.3	753.6							
	399.4	18.7	751.2							
0.798	360.1	12.2	743.5	0.10209	−24.3802	0.991		−0.2161	823.8959	0.529
	370.8	13.7	748.3							
	381.7	14.5	738.6							
	391.0	15.6	741.8							
	401.0	16.4	735.7							
0.826	358.6	10.5	748.1	0.08537	−20.2225	0.996		−0.2126	823.5450	0.906
	367.1	11.0	736.5							
	376.7	11.9	741.7							
	388.0	12.9	741.6							
	398.7	13.9	739.2							

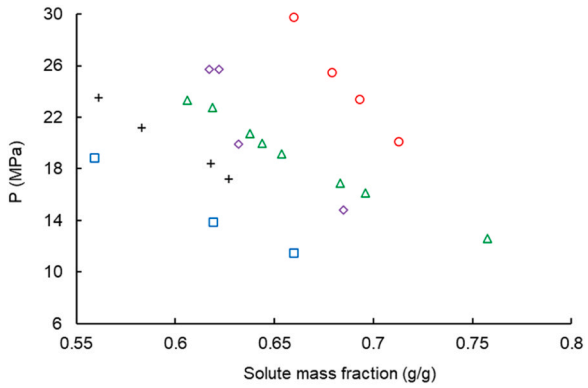

Fig. 9. Comparison of data for Wax 1 at 348.2 K with phase transition data for *n*-alkane binary mixtures at similar temperatures [14] (Key: Δ = Wax 1 (this work), □ = C20, measured at 348.3 K, + = C24, measured at 348.1 K, ◊ = C28, measured at 348.0 K and ○ = C36, measured at 348.5 K [14]).

with the error in predicted pressures provided by the correlations well below a 2 % deviation. Increasing the order of the fit did not improve the prediction.

The bubble point pressures, the calculated densities and viscosities for the system Wax 1 + CO_2 are provided in Table 2, and the impact of the mixture wax mass fraction on phase transition pressure is graphically illustrated in Fig. 7. Phase transitions were determined between 318 K and 358 K for Wax 1 as informed by the melting experiments.

The phase transition pressure increases with increasing temperature in the high wax fraction regions. As the CO_2 concentration increases, the phase transition pressure starts to decrease with increasing temperature, and a temperature inversion is observed, similar to temperature inversions previously documented in binary mixtures of CO_2 and pure *n*-alkanes with carbon number greater than 16 [14], and 1-hexadecanol [60]. It is also evident from Fig. 7 that the solubility of CO_2 in Wax 1 increases with increasing pressure and decreasing temperature (up until the temperature inversion point), similar to what was seen for binary CO_2 mixtures with *n*-alkanes [14], tristearin and rapeseed oil [61], and complex lipid carriers [62]. This is due to the decrease in density (and increase in vapour pressure) and thus solvent power of the CO_2 as temperature increases.

The phase transition pressure also decreases with increased wax content and approaches zero (wax vapour pressure) at $X_{wax} = 1$. A similar phenomenon was observed for the phase behaviour of binary mixtures of CO_2 and higher molecular weight *n*-alkanes [14], hardened rapeseed oil, tripalmitin and hydrogenated castor oil (HCO) [63], and polydimethylsiloxane (PDMS) [32].

The phase behaviour of Wax 2 was investigated between 358.2 K and 398.2 K (see Fig. 8). The data are provided in Table 3. As with the more concentrated mixtures of Wax 1, the phase transition pressure increases with increasing temperature, and decreases with increased wax concentration. As the wax mass fraction decreases, the impact of temperature on phase transition pressure decreases. This suggests that a temperature inversion might also be present for Wax 2, but at lower wax mass fractions and/or temperatures than considered in this work.

The reduced impact of temperature on the wax solubility of CO_2 at lower wax concentrations appears contrary to the impact of temperature on the density (and thus solvent power) of pure CO_2 at similar

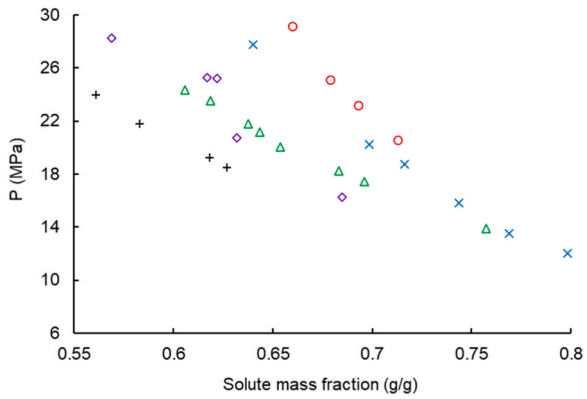

Fig. 10. Comparison of data for Wax 1 at 358.2 K with phase transition data for *n*-alkane binary mixtures at similar temperatures [14] (Key: Δ = Wax 1 (this work), x = Wax 2 (this work), + = C24,measured at 357.1 K, ◊ = C28, measured at 357.0 K, and ○ = C36, measured at 357.0 K [14]).

conditions. This can be attributed to the dominance of the pressure effect over changes in solvent power of pure CO_2 as a result of temperature changes.

The phase transition pressures of Wax 2 are greater than those for Wax 1 in mixtures with similar wax mass fractions. The increased chain lengths of the wax result in phase separation occurring at higher pressures, and thus the narrowing of the window of composition that can be measured before the phase transition surpasses the 30 MPa equipment limit. This increase in phase transition pressure due to an increase in carbon number has also previously been seen in *n*-alkanes [14].

Comparisons of the phase behaviour of Wax 1 and Wax 2 to the phase behaviour for *n*-alkanes [14] around 348 K and 358 K are shown in Fig. 9 and Fig. 10 respectively. In Fig. 9 it is shown that the phase transition pressures of Wax 1 lie between that of C28 and C36. The phase transition behaviour of waxes is determined by their carbon number distribution and the degree of chain length disorder, with the phase behaviour expected to match that of the pure *n*-alkane closest to the average chain length of the wax [64]. The phase behaviour of Wax 1 (457.5 g/mol) at 348.2 K behaves between that of C28 (394.8 g/mol) and C36 (507.0 g/mol), closer to the former, in agreement with the previous argument.

In Fig. 10, even though there is a greater difference in the temperatures at which the *n*-alkanes were measured as compared to both Wax 1 and Wax 2, Wax 1 still behaves as expected. The phase transition pressures of Wax 2 (M_w = 546.1 g/mol) are slightly lower than that of C36, even though Wax 2 has a slightly higher M_w. This could be as a result of the wider chain length distribution of Wax 2 (with a broader DSC melting peak) deviating more from the behaviour of a similar average carbon number *n*-alkane, or as a result of the greater impact of temperature on phase behaviour of Wax 2 at these conditions.

These results align with the differences in the melting behaviours of Wax 1, Wax 2 and Wax 3. As stated, the solubility of CO_2 in Wax 1 is greater than in Wax 2 and Wax 3 at comparable pressure, and thus allows for easier entrainment of mobile amorphous and short chain components into the CO_2 phase. A highly homogeneous crystalline phase remains that crystallises under increased pressure.

The phase behaviour for Wax 3 is shown in Fig. 11 and the data provided in Table 4. As with the lower melting point waxes, the phase transition pressure increases as the mass fraction of wax is decreased and as the temperature increases. Again, the phase transition pressure increases for Wax 3 as compared to Wax 2 (and Wax 1), with the operating limit of the equipment reached at a mixture wax mass fraction of 0.73 for the highest temperatures tested.

3.3. Density

The approach outlined for correlation and generation of isothermal data for comparison between mixtures during the phase behaviour studies was also applied to the density-temperature data for each mixture. The data for Wax 1 could all be correlated to $R^2 > 0.99$, while the density data for all of the Wax 3 mixtures could be linearly correlated to $R^2 > 0.95$, with the error in the predicted data well below 2 % for all mixtures. Generally, the density data for all Wax 2 mixtures could be correlated linearly to $R^2 > 0.90$, with error in predicted values below 0.6 % at all temperatures measured. Increasing the order of the fit to a 2nd or even 3rd order polynomial did not greatly increase the R^2 value but did result in increased error in the predicted values of the density data for Wax 2 and Wax 3.

The densities of the Wax 1 + CO_2 mixtures (as measured in the single-phase region just above the phase transition point) decrease with increasing temperature (see Fig. 12), which is expected behaviour for fluids. The impact of temperature on the density of the mixture increases as the wax mass fraction decreases. Density also decreases as the wax content of the mixture is increased, similar to what was observed with binary mixtures with *n*-alkanes [14]. This behaviour is in line with the density of pure CO_2 at similar pressure and temperature ranges and comparable to the trends in CO_2 solubility shown for Wax 1 at higher temperatures.

Lower densities were determined for Wax 2 + CO_2, as the higher melting temperatures required for Wax 2 results in lower CO_2 density.

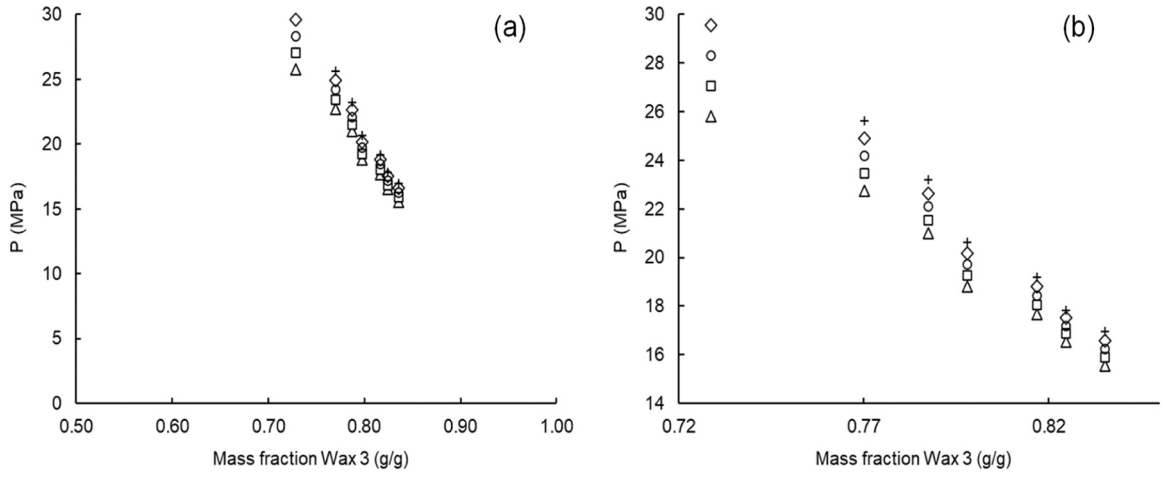

Fig. 11. Pressure-composition data for Wax 3 + CO_2 (a) between 0 MPa and 30 MPa and a wax mass fraction of 0.5–1 and (b) between 14 MPa and 30 MPa and a wax mass fraction of 0.72 and 0.83 (Key: Δ = 378.20 K, □ = 383.20 K, ○ = 388.20 K, ◊ = 393.20 K and + = 398.20 K).

Table 4
Experimental phase behaviour data (temperature (T) and pressure (P)) for the system CO_2 + Wax 3 at various wax concentrations (X_{wax}), as well as density (ρ) measured at the phase transition.

X_{wax} [g/g]	T [K]	P [MPa]	ρ (kg/m^3)	Pressure-Temperature relationship, P = AT+B with P in MPa and T in K			Density - Temperature relationship, ρ = AT + B with ρ in kg/m^3 and T in K		
				A	B	R	A	B	R
0.729	378.5	25.9	811.4	0.2514	−69.2656	0.983	−0.1573	870.7629	0.965
	383.2	26.9	810.2						
	388.3	28.6	Not measured						
	393.4	29.5	808.9						
0.770	378.7	22.8	815.2	0.1436	−31.5453	0.997	−0.3707	955.6446	0.991
	383.2	23.5	813.6						
	388.0	24.1	811.8						
	392.8	24.9	810.5						
	397.9	25.6	807.9						
0.787	378.0	20.9	815.3	0.1098	−20.5209	0.996	−0.5834	1035.8570	0.972
	382.8	21.5	811.7						
	389.5	22.3	809.9						
	394.0	22.7	806.4						
	400.4	23.4	801.5						
0.798	377.7	18.8	797.9	0.0926	−16.2168	0.960	−0.7444	1078.5475	0.952
	383.5	19.3	793.5						
	388.5	19.6	789.0						
	392.3	19.9	784.5						
	398.4	20.8	783.5						
0.817	377.7	17.6	816.0	0.0748	−10.5984	0.991	−0.8002	1118.8435	0.994
	383.9	18.1	812.2						
	388.6	18.5	808.2						
	393.3	18.9	804.5						
	399.3	19.2	798.8						
0.825	378.2	16.5	806.6	0.0644	−7.8111	0.994	−0.8854	1141.5705	1.000
	383.6	16.9	802.2						
	386.9	17.1	799.0						
	391.1	17.4	795.2						
	398.4	17.8	788.8						
0.835	377.3	15.4	806.0	0.0697	−10.8162	0.991	−0.9936	1181.8821	0.984
	382.9	15.9	802.1						
	387.1	16.2	798.1						
	391.5	16.5	793.8						
	397.6	16.8	785.8						

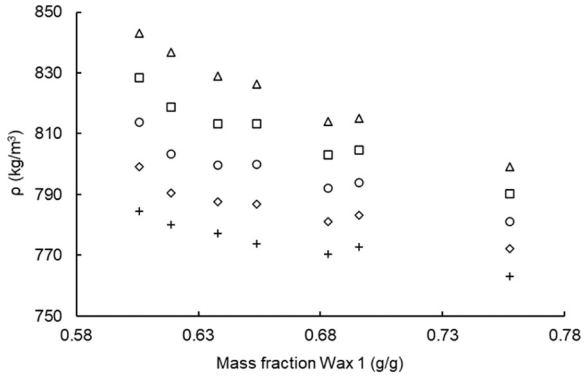

Fig. 12. Density-composition data for Wax 1 +CO_2 (Key: Δ = 318.15 K, □ = 328.15 K, ○ = 338.15 K, ◇ = 348.15 K and + = 358.20 K).

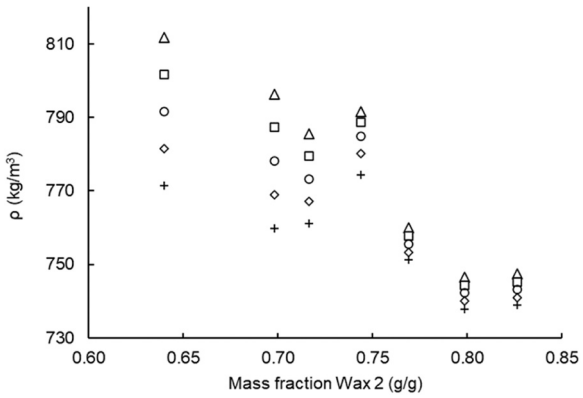

Fig. 13. Density-composition data for Wax 2 +CO_2 (Key: Δ = 358.20 K, □ = 368.20 K, ○ = 378.20 K, ◇ = 388.20 K and + = 398.20 K).

Similarly to Wax 1, the impact of temperature on the density of the CO_2 + Wax 2 mixtures increases as the amount of CO_2 in the mixture increases, with a difference of approximately 40 kg/m^3 between the densities determined at 358.2 K and at 398.2 K, as shown in Fig. 13. Again, this behaviour mimics that of pure CO_2 at the respective phase transition pressures and temperatures, with the impact of pressure on density less pronounced at higher temperatures.

For Wax 3, the lower the mass fraction of wax in the mixture, the less density is influenced by temperature, as can be seen in Fig. 14. This corresponds to the impact of temperature on pure CO_2 density at these conditions, with density virtually equal for all temperatures at this mixture composition.

The negligible impact of temperature on density at the less concentrated wax mixtures could be due to domination of the compression effect over the impact of temperature. As the wax mass fraction in the mixture increases (and the phase transition pressure decreases), the impact of temperature on the measured densities increases. Density generally decreases with increasing wax mass fraction at higher temperatures, similar to the corresponding pure CO_2 density values. The impact is less pronounced at the lower temperatures measured, where phase transition pressures are the lowest. For all three waxes, density increases slightly at intermediate wax concentration before decreasing further with increasing wax concentration. As CO_2 content in the

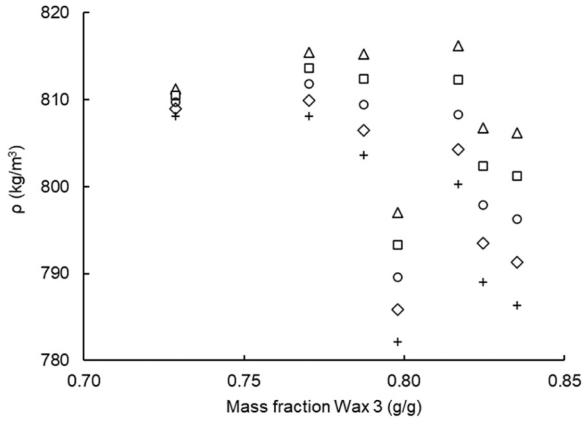

Fig. 14. Density-composition data for Wax 3 +CO_2 (Key: Δ = 378.20 K, □ = 383.20 K, ○ = 388.20 K, ◇ = 393.20 K and + = 398.20 K).

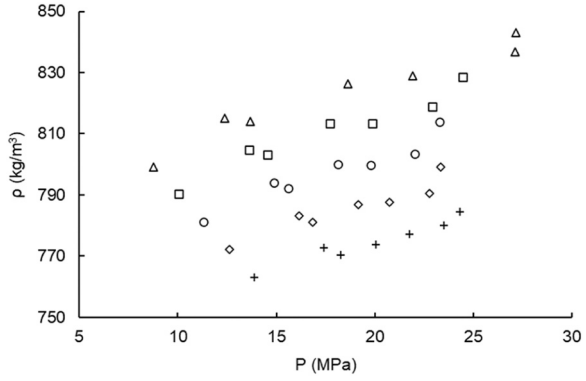

Fig. 15. Density-pressure data for Wax 1 +CO_2 (Key: Δ = 318.15 K, □ = 328.15 K, ○ = 338.15 K, ◇ = 348.15 K and + = 358.20 K).

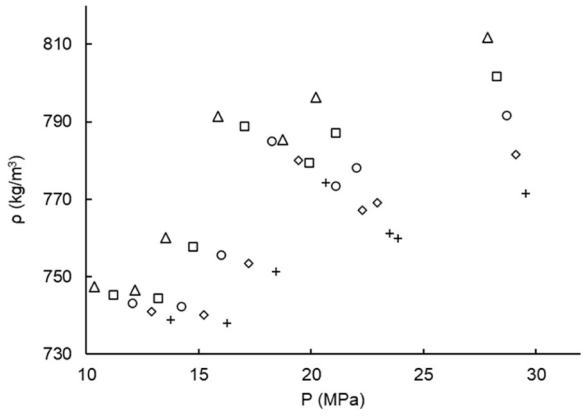

Fig. 16. Density-pressure data for Wax 2 +CO_2 (Key: Δ = 358.20 K, □ = 368.20 K, ○ = 378.20 K, ◇ = 388.20 K and + = 398.20 K).

mixture increases, more CO_2 is dissolved in the wax, resulting in increased density. At a certain concentration, the space in between wax molecules available for CO_2 becomes fully occupied, and a slight decrease in density is observed. As the CO_2 content is further increased, the density once again increases as the CO_2 behaviour in the mixture becomes dominant.

Overall, the change in density with temperature and composition decreases with increasing chain length (Wax 1 > Wax 2 > Wax 3) as experimental conditions move further away from the CO_2 critical point,

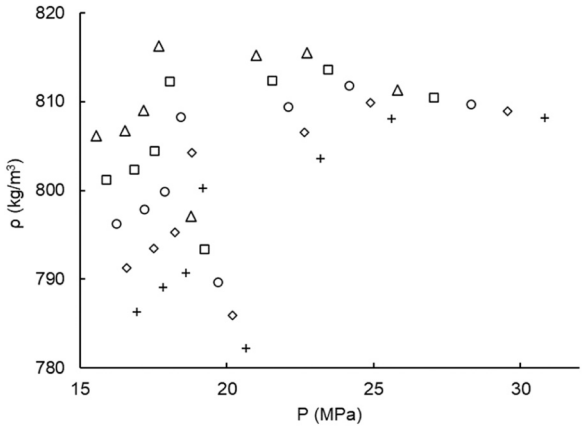

Fig. 17. Density-pressure data for Wax 3 +CO_2 (Key: Δ = 378.20 K, □ = 383.20 K, ○ = 388.20 K, ◇ = 393.20 K and + = 398.20 K).

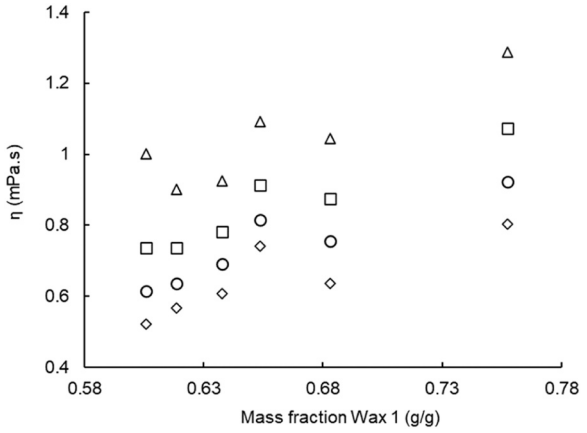

Fig. 18. Viscosity-composition data for Wax 1 + CO_2 (Key: Δ = 318.15 K, □ = 328.15 K, ○ = 338.15 K and ◇ = 348.15 K).

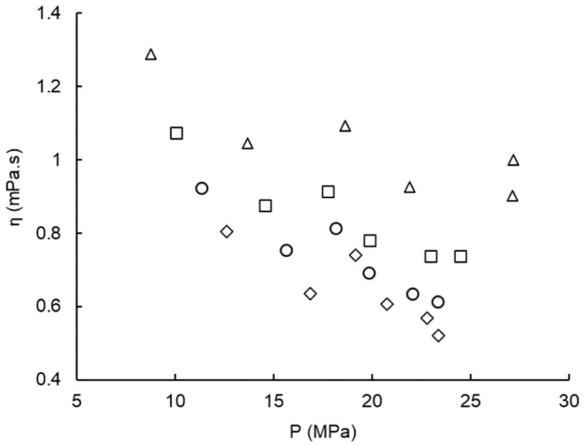

Fig. 19. Viscosity-pressure data for Wax 1 + CO_2 (Key: Δ = 318.15 K, □ = 328.15 K, ○ = 338.15 K and ◇ = 348.15 K).

and also due to the smaller temperature gradient (as compared to Wax 1 and Wax 2) under which Wax 3 was measured.

When comparing the density of the mixtures to phase transition pressures, the density of Wax 1 increases linearly with increased pressure, and increases with decreasing temperature (see Fig. 15). This is also observed for Wax 2 in Fig. 16, but with a less linear relationship

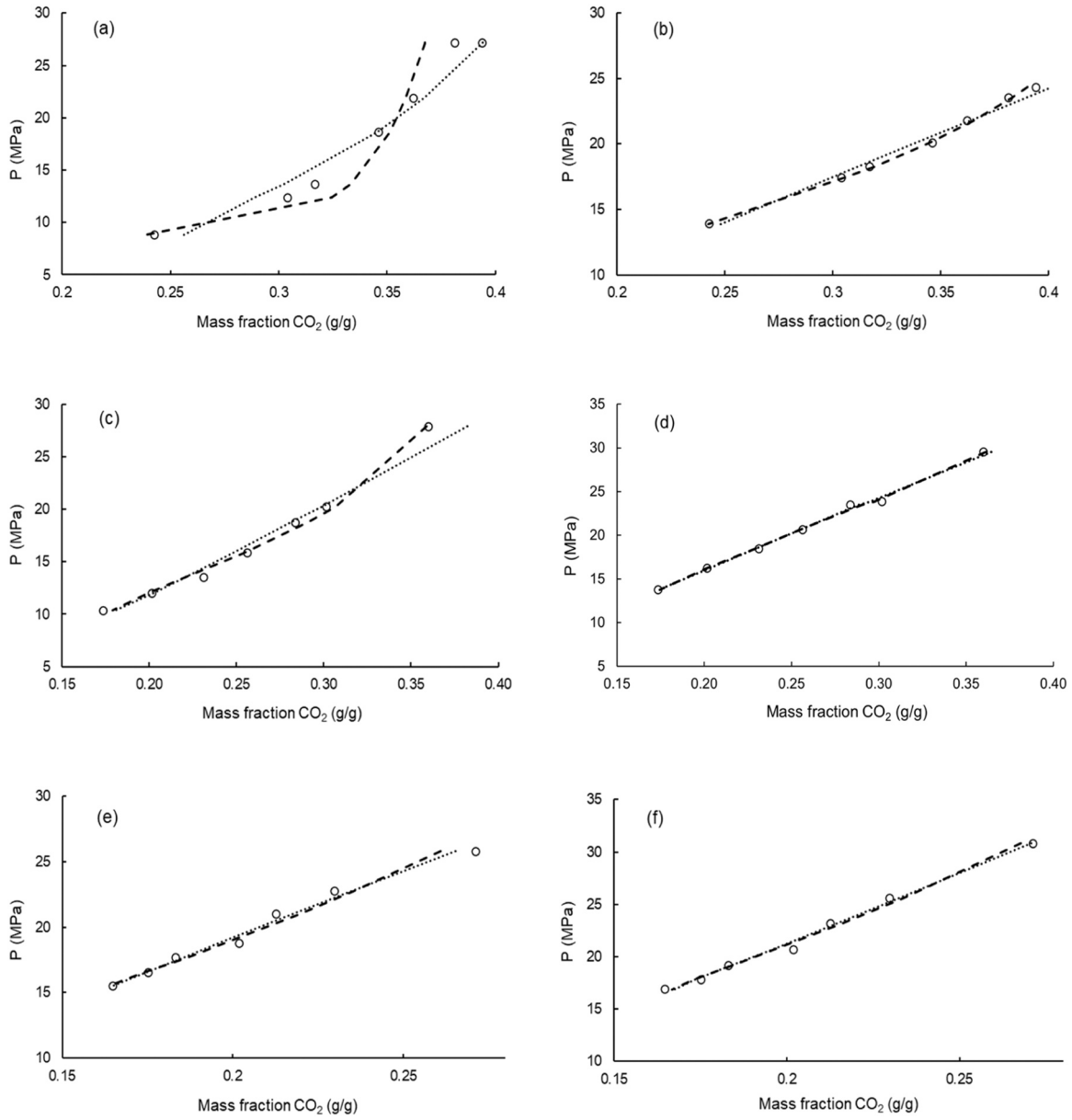

Fig. 20. Comparison of solubility data (g CO_2/ g mixture) as measured and predicted by both approaches of the modified Chrastil model for CO_2 in (a) Wax 1 at 318.15 K, (b) in Wax 1 at 348.15 K, (c) in Wax 2 at 358.20 K, (d) in Wax 2 at 398.20 K, and (e) in Wax 3 at 378.20 K and (f) in Wax 3 at 398.20 K (Key: ○ = experimental data, dotted line: lnρ/P approach and dashed line: lnρ approach).

between pressure and density, and with the impact of pressure on density tapering off at low pressures. Similar behaviour is observed for the corresponding pure CO_2 densities and was also observed in binary CO_2 mixtures with tristearin and rapeseed oil [61]. A slightly sharper increase in density is seen at higher pressures, more likely due to compression effects rather than increasing CO_2 solubility [61].

The impact of temperature on the density of the mixtures is however much more pronounced at higher pressures, similar to the impact of temperature on the density of pure CO_2 at these pressures.

The densities of the CO_2 + Wax 3 mixtures (shown in Fig. 17) are much less affected by changes in temperature and pressure than the densities of the mixtures of Wax 1 and Wax 2 with CO_2 respectively, suggesting a high degree of incompressibility of the wax. At high pressures, temperature barely affects the mixture density.

3.4. Viscosity

The relationship between the measured viscosity and mixture composition of Wax 1 + CO_2 is shown in Fig. 18. Due to the limitations of the viscosity range of the equipment available for this study, the viscosities of Wax 2 and Wax 3 could not be measured. The high viscosities of the Wax 2 and Wax 3 mixtures meant that damping occurred to such an extent that the electrical response of the quartz crystal, and thus viscosity, could not be measured accurately. Future work may include modification of the current set-up or construction of an alternative setup to allow for measurement of higher viscosity mixtures.

The viscosities of the mixtures generally increased with an increase in wax content, and decreased with temperature, similarly to what was observed for mixtures of PDMS and CO_2 [32].

The impact of pressure on viscosity is more complicated, as shown in Fig. 19. At lower pressures (and thus more concentrated wax mixtures) viscosity decreased with an increase in pressure and an increase in

Table 5
Parameters and fit of modified Chrastil correlation to the solubility data for binary mixtures of CO_2 and the three waxes.

XCO_2 range	T [K]	lnρ				lnρ/P			
Wax 1		**A**	**B**	**R^2**	**%AAD**	**A**	**B**	**R^2**	**%AAD**
0.727–0.844	318.2	0.1132	−0.9196	0.929	0.925	−0.2691	−0.0709	0.943	0.736
	328.2	0.1365	−1.0613	0.966	0.649	−0.3849	−0.0278	0.962	0.666
	338.2	0.1561	−1.1764	0.986	0.411	−0.5226	0.0156	0.974	0.562
	348.2	0.1781	−1.3066	0.995	0.232	−0.6504	0.0467	0.982	0.480
	358.2	0.2016	−1.4457	0.999	0.118	−0.7834	0.0745	0.985	0.443
Wax 2									
0.757–0.893	358.2	0.1587	−1.1737	0.987	0.543	−0.6594	0.0332	0.978	0.758
	368.2	0.1753	−1.2709	0.993	0.382	−0.7516	0.0487	0.985	0.646
	378.2	0.1929	−1.3734	0.995	0.362	−0.8441	0.0626	0.991	0.508
	388.2	0.2084	−1.4629	0.997	0.309	−0.9406	0.0765	0.995	0.389
	398.2	0.2256	−1.5625	0.998	0.219	−1.0338	0.0884	0.998	0.254
Wax 3									
0.828–0.900	378.2	0.1671	−1.1935	0.981	0.399	−0.7437	0.0557	0.987	0.306
	383.2	0.1646	−1.1761	0.986	0.336	−0.7329	0.0458	0.989	0.294
	388.2	0.1613	−1.1538	0.987	0.329	−0.7256	0.0373	0.990	0.279
	393.2	0.1587	−1.1364	0.989	0.314	−0.7193	0.0297	0.990	0.270
	398.2	0.1553	−1.1139	0.988	0.318	−0.7158	0.0233	0.989	0.261

Table 6
Parameters and fit of modified Chrastil correlation to the solubility data for binary mixtures of CO_2 and *n*-alkanes of increasing chain length [14].

XCO_2 range	T [K]	lnρ				lnρ/P			
C20		**A**	**B**	**R^2**	**%AAD**	**A**	**B**	**R^2**	**%AAD**
0.767–0.878	315.9	0.0778	−0.6965	0.823	1.598	−0.2549	−0.0798	0.976	0.667
	320.6	0.0970	−0.8168	0.885	1.394	−0.3180	−0.0525	0.976	0.647
	329.6	0.1511	−1.1522	0.962	0.826	−0.4294	−0.0141	0.971	0.788
	339.1	0.1337	−1.0265	0.953	1.033	−0.5025	0.0081	0.989	0.448
	348.3	0.1277	−0.9516	0.924	1.062	−0.4606	0.0099	0.944	0.967
C24									
0.827–0.862	329.7	0.1986	−1.4808	0.966	0.246	−0.2690	−0.0798	0.983	0.175
	339.2	0.2008	−1.4771	0.991	0.122	−0.3865	−0.0417	0.997	0.090
	348.1	0.1863	−1.3681	0.981	0.201	−0.4846	−0.0143	0.993	0.111
	357.1	0.2000	−1.4448	0.999	0.041	−0.6438	0.0276	0.998	0.091
C28									
0.819–0.856	338.5	0.0970	−0.8018	0.981	0.198	−0.2108	−0.1028	0.932	0.393
	348.0	0.0937	−0.7714	0.972	0.243	−0.2661	−0.0861	0.919	0.429
	357.0	0.1285	−0.9857	0.898	0.596	−0.4146	−0.0426	0.910	0.733
	366.4	0.2198	−1.5819	0.899	0.509	−0.3755	−0.0584	0.915	0.425
C36									
0.845–0.871	344.0	0.1565	−1.1839	0.987	0.086	−0.2936	−0.0744	0.992	0.069
	348.5	0.1536	−1.1587	0.994	0.071	−0.3166	−0.0677	0.999	0.034
	357.0	0.1439	−1.0851	0.999	0.036	−0.3620	−0.0560	0.996	0.064
	366.9	0.1449	−1.0809	0.990	0.095	−0.4388	−0.0373	0.982	0.126

Table 7
Results of the Mendez-Santiago & Teja correlation applied to the solubility data of the waxes as well as the *n*-alkanes measured by [14].

	A	**B**	**C**	**R^2**	**%AAD**
Wax 1	−2031.64	0.7274	21.19	0.938	6.407
Wax 2	−1597.76	0.9665	19.66	0.981	3.769
Wax 3	−1613.66	0.9771	19.73	0.997	0.979
C20	−2087.54	0.6632	21.51	0.937	8.523
C24	−2765.11	1.0002	22.79	0.987	1.955
C28	−1553.45	0.8273	19.64	0.916	5.419
C36	−2548.14	1.0160	22.13	0.996	0.989

temperature, in a relatively linear manner. This is due to the increase of the CO_2 solubility in the wax, similar to what was observed for tristearin and rapeseed oil [61].

Between 17.5 MPa and 19 MPa there is a slight increase in viscosity at all of the experimental temperatures as pressure increases. This is in the pressure region where the temperature inversion in the phase behaviour of Wax 1 was observed (see Fig. 7).

Thereafter the viscosity decreases slightly or does not change significantly as the pressure is further increased. The increase in the solubility of CO_2 in the wax as the pressure increases is thus offset by the compression effect at higher pressure. This was also observed for viscosity of cocoa butter [38] and canola oil [65]. At 318.2 K there is an increase in viscosity around 27 MPa, indicative of the domination of compression effects over increased solubility.

3.5. Correlation of solubility data

The modified Chrastil [66] and Mendez-Santiago & Teja [67] models were applied to correlate the solubility data of sc-CO_2 in the waxes. The original Chrastil correlation was developed to correlate the solubility of a solute in a supercritical fluid to the density of the supercritical fluid [68]. It was subsequently shown that the Chrastil correlation could also be applied to the solubility of a supercritical fluid in the solute phase, by adjusting for systems with positive and negative deviations from Henry's Law respectively [66].

The modified Chrastil model allows for correlation of the solubility of CO_2 in lower weight solutes, where positive deviations from Henry's Law occur (Eq. 3), as well as the solubility of CO_2 in heavy weight solutes, with negative deviations from Henry's law (Eq. 4) [66].

$$\ln X_{CO2} = A\ln\rho_{CO2} + B \tag{3}$$

$$\ln X_{CO2} = A' \frac{\ln \rho_{CO2}}{P} + B' \quad (4)$$

The modified Chrastil correlations have been applied to correlate the solubility of CO_2 in a wide range of compounds from literature [66,69].

Both approaches were applied to each of the three waxes, in order to assess which is most suitable, with suitability judged by how closely the approach mimics a linear relationship. The results are illustrated in Fig. 20 and shown in Table 5. When comparing the linear fit in general for Wax 1, the approach of correlating against lnρ gave the best results, with the higher R^2 values and lower %AAD when compared to the lnρ/P approach. The lnρ/P approach at 318.2 K gives a better linear fit and smaller error in the predicted solubility of CO_2 in Wax 1. The two approaches give a very similar quality of fit at 328.2 K, whereafter, with increasing temperature, the lnρ approach increasingly provides a more accurate fit to the data.

For the solubility of CO_2 in Wax 2, a better linear fit in general was provided by the lnρ approach. As with Wax 1, the linear fit improved with increasing temperature, with the quality of fit for both approaches converging at higher temperatures. In the case of Wax 3, the lnρ/P approach provided a better overall linear fit, but the differences in the R^2 values for the two approaches are very small. Thus, as the melting points of the waxes increase, the quality of the fit provided by the two approaches converges and the impact of temperature on the quality of the fit decreases.

The two approaches were also applied to data published for binary mixtures of CO_2 and longer chain *n*-alkanes [14]. The parameters and quality of fit determined for C20, C24, C28 and C36 *n*-alkane binary mixtures with CO_2 are shown in Table 6. For the C36 *n*-alkane data, both approaches showed a good linear correlation with high R^2 values, and smaller errors in the predicted solubilities of CO_2 in the *n*-alkane than what was determined for the waxes.

The Mendez-Santiago & Teja correlation (Eq. 5) was also originally developed for the modelling of the solubility of solids in supercritical fluids [67]. The model has since been applied to the solubility of CO_2 in dicarboxylic acid esters [70] and ethyl esters [71].

The model was also applied to the experimental data, with the results shown in Table 7.

$$T\ln(X_{CO2}P) - CT = A' + \quad B'\rho_{CO2} \quad (5)$$

As with the modified Chrastil correlation, the linear fit as well as the average error in the predicted versus the experimental results improved/decreased as the molecular weight of the wax increased.

The fit and accuracy of the predicted solubility of CO_2 for Wax 1 is improved by discounting the data for the two lowest temperatures. This can be explained by the temperature inversion that is observed in the phase behaviour of Wax 1, with a greater pressure difference with changes in mixture composition at the lower temperatures.

4. Conclusion

The melting temperatures of Wax 1 and Wax 2 both increased slightly with increased pressure due to domination of the hydrostatic pressure effect. A slight decrease in melting temperature was observed for the oxidised Wax 3. The more mobile chains and increased solubility of CO_2 in Wax 1 resulted in pressure induced crystallisation above certain pressure conditions.

For all three waxes, the phase transition pressure increased with increasing temperature and decreasing wax content, with solubility of CO_2 in the solute varying accordingly. A temperature inversion was seen for the lowest melting point wax (Wax 1). An increase in average carbon number/molecular weight of the waxes resulted in an increase in phase transition pressures. The impact of temperature and pressure on the density of the binary mixtures of the waxes and CO_2 was similar to the impact on pure CO_2 density, and accordingly the influence of process conditions on density was reduced the further away the conditions deviated from the critical point. The general phase behaviour of Wax 1 and Wax 2 could be compared relatively well to the *n*-alkanes of similar average carbon number. The viscosity of Wax 1 increased with increased wax content and decreasing temperature. The viscosity decreased as the pressure increased, up to the temperature inversion point, whereafter further increasing pressure had little effect on the viscosity, with the compression effect nullifying the effect of increasing CO_2 solubility. Equipment modification or the use of alternative methods will be investigated in the future to determine the viscosities of Wax 2 + CO_2 and Wax 3 + CO_2.

The modified Chrastil correlation could model the solubility of CO_2 in the wax phase within 1 % of the measured values for all three waxes, while the accuracy of the Mendez-Santiago & Teja correlation increased as the molecular weight of the wax increased, with comparable accuracy to the modified Chrastil correlation for Wax 3.

Although the melting temperatures of Fisher-Tropsch waxes were not appreciably reduced by sc-CO_2 over the experimental conditions, solubility of CO_2 in the waxes was influenced by changes in processing conditions. This suggests that there is potential for the optimisation of PGSS parameters to obtain micronised Fischer-Tropsch waxes with targeted particle sizes and morphologies.

CRediT authorship contribution statement

Swanepoel Andri: Writing – original draft, Validation, Methodology, Investigation, Formal analysis, Conceptualization. **Labuschagne Philip W.:** Writing – review & editing, Supervision, Funding acquisition, Conceptualization. **Schwarz Cara:** Writing – review & editing, Supervision, Project administration, Data curation, Conceptualization.

Declaration of Competing Interest

The authors declare that they have no known competing financial interests or personal relationships that could have appeared to influence the work reported in this paper.

Acknowledgements

The authors would like to thank Dr Carla Latsky-Galloway as well as Ms O. Hillary Jayeola for their assistance in optimising the experimental methods and generation of the high-pressure phase behaviour data. The authors would also like to thank Prof Ray Suprakas, the Council for Scientific and Industrial Research and the Department of Science and Innovation for funding of this work.

Data availability

All data are available in the manuscript

References

[1] Ž. Knez, M. Knez Hrnčič, M. Škerget, Particle formation and product formulation using supercritical fluids, Annu. Rev. Chem. Biomol. Eng. 6 (2015) 379–407, https://doi.org/10.1146/annurev-chembioeng-061114-123317.
[2] Z. Knez, E. Weidner, Particles formation and particle design using supercritical fluids, Curr. Opin. Solid State Mater. Sci. 7 (2003) 353–361, https://doi.org/10.1016/j.cossms.2003.11.002.
[3] E. Weidner, Ž. Knez, Z. Novak, Eur. Pat. EP 0744 (992) (1995) 0744992.
[4] S. Klettenhammer, G. Ferrentino, H.S. Zendehbad, K. Morozova, M. Scampicchio, Microencapsulation of linseed oil enriched with carrot pomace extracts using Particles from Gas Saturated Solutions (PGSS) process, J. Food Eng. 312 (2022) 110746, https://doi.org/10.1016/J.JFOODENG.2021.110746.
[5] T. Hatami, J. Yang, M.A.A. Meireles, O.N. Ciftci, Sensitivity analysis of the formation of hollow solid lipid micro- and nanoparticles from CO_2-saturated solution of fully hydrogenated soybean oil, Powder Technol. 435 (2024) 119189, https://doi.org/10.1016/J.POWTEC.2023.119189.
[6] O.N. Ciftci, F. Temelli, Melting point depression of solid lipids in pressurised carbon dioxide, J. Supercrit. Fluids 92 (2014) 208–214, https://doi.org/10.1016/J.SUPFLU.2014.05.009.

[7] J. de Swaan Arons, G.A.M. Diepen, Thermodynamic study of melting equilibria under pressure of a supercritical gas, Recl. Trav. Chim. Pays-Bas 82 (1963) 249–256, https://doi.org/10.1002/recl.19630820308.

[8] S.G. Kazarian, C.J. Lawrence, B.J. Briscoe, In-situ spectroscopy of polymers processed with supercritical carbon dioxide, SPIE 4060 (1999) 210–216, https://doi.org/10.1117/12.375295.

[9] S.G. Kazarian, M.F. Vincent, F.V. Bright, C.L. Liotta, C.A. Eckert, Specific intermolecular interaction of carbon dioxide with polymers, J. Am. Chem. Soc. 118 (1996) 1729–1736, https://doi.org/10.1021/ja950416q.

[10] S.P. Nalawade, F. Picchioni, L.P.B.M. Janssen, Supercritical carbon dioxide as a green solvent for processing polymer melts: processing aspects and applications, Prog. Polym. Sci. 31 (2006) 19–43, https://doi.org/10.1016/j.progpolymsci.2005.08.002.

[11] M.K. Hrnčič, M. Škerget, Ž. Knez, Density and viscosity of the binary polyethylene glycol/CO_2 systems, J. Supercrit. Fluids 95 (2014) 641–668, https://doi.org/10.1016/j.supflu.2014.09.045.

[12] K. Chandler, F.L.L. Pouillot, C.A. Eckert, Phase equilibria of alkanes in natural gas systems. 3. alkanes in carbon dioxide, J. Chem. Eng. Data 41 (1996) 6–10, https://doi.org/10.1021/je950138a.

[13] V.S. Smith, P.O. Campbell, V. Vandana, A.S. Teja, Solubilities of long-chain hydrocarbons in carbon dioxide, Int. J. Thermophys. 17 (1996) 23–33, https://doi.org/10.1007/BF01448206.

[14] I. Nieuwoudt, M. du Rand, Measurement of phase equilibria of supercritical carbon dioxide and paraffins, J. Supercrit. Fluids 22 (2002) 185–199, https://doi.org/10.1016/S0896-8446(01)00122-X.

[15] T. Furuya, A.S. Teja, The solubility of high molecular weight n-alkanes in supercritical carbon dioxide at pressures up to 50 MPa, J. Supercrit. Fluids 29 (2004) 231–236, https://doi.org/10.1016/S0896-8446(03)00088-3.

[16] M.A. McHugh, A.J. Seckner, T.J. Yogan, High-pressure phase behaviour of binary mixtures of octacosane and carbon dioxide, Ind. Eng. Chem. Fundam. 23 (1984) 493–499, https://doi.org/10.1021/i100016a020.

[17] E. Reverchon, P. Russo, A. Stassi, Solubilities of solid octacosane and triacontane in supercritical carbon dioxide, J. Chem. Eng. Data 38 (1993) 458–460, https://doi.org/10.1021/je00011a034.

[18] Y. Sato, K. Fujiwara, T. Takikawa, Sumarno, S. Takishima, H. Masuoka, Solubilities and diffusion coefficients of carbon dioxide and nitrogen in polypropylene, high-density polyethylene, and polystyrene under high pressures and temperatures, Fluid Phase Equilib. 162 (1999) 261–276, https://doi.org/10.1016/S0378-3812(99)00217-4.

[19] D. Čuček, T. Perko, L. Ilić, B. Znoj, P. Venturini, Ž. Knez, M. Škerget, Phase equilibria and diffusivity of dense gases in various polyethylenes, J. Supercrit. Fluids 78 (2013) 54–62, https://doi.org/10.1016/J.SUPFLU.2013.03.020.

[20] F. Sarrasin, P. Memari, M.H. Klopffer, V. Lachet, C. Taravel Condat, B. Rousseau, E. Espuche, Influence of high pressures on CH_4, CO_2 and H_2S solubility in polyethylene: experimental and molecular simulation approaches for pure gas and gas mixtures. Modelling of the sorption isotherms, J. Memb. Sci. 490 (2015) 380–388, https://doi.org/10.1016/J.MEMSCI.2015.04.040.

[21] Z. Feng, S.R. Panuganti, W.G. Chapman, Predicting solubility and swelling ratio of blowing agents in rubbery polymers using PC-SAFT Equation of State, Chem. Eng. Sci. 183 (2018) 306–328, https://doi.org/10.1016/J.CES.2018.03.024.

[22] G. Li, H. Li, J. Wang, C.B. Park, Investigating the solubility of CO_2 in polypropylene using various EOS models, Cell. Polym. 25 (2006) 237–248, https://doi.org/10.1177/026248930602500403.

[23] Z. Lei, H. Ohyabu, Y. Sato, H. Inomata, R.L. Smith, Solubility, swelling degree and crystallinity of carbon dioxide–polypropylene system, J. Supercrit. Fluids 40 (2007) 452–461, https://doi.org/10.1016/J.SUPFLU.2006.07.016.

[24] M.M. Hasan, Y.G. Li, G. Li, C.B. Park, P. Chen, Determination of solubilities of CO_2 in linear and branched polypropylene using a magnetic suspension balance and a PVT apparatus, J. Chem. Eng. Data 55 (2010) 4885–4895, https://doi.org/10.1021/je100488v.

[25] P. Kundra, S.R. Upreti, A. Lohi, J. Wu, Experimental determination of composition-dependent diffusivity of carbon dioxide in polypropylene, J. Chem. Eng. Data 56 (2011) 21–26, https://doi.org/10.1021/je100622u.

[26] J. Hou, G. Zhao, G. Wang, L. Zhang, G. Dong, B. Li, Ultra-high expansion linear polypropylene foams prepared in a semi-molten state under supercritical CO_2, J. Supercrit. Fluids 145 (2019) 140–150, https://doi.org/10.1016/J.SUPFLU.2018.11.017.

[27] J.C. Crause, I. Nieuwoudt, Fractionation of paraffin wax mixtures, Ind. Eng. Chem. Res. 39 (2000) 4871–4876, https://doi.org/10.1021/ie000249p.

[28] G.J. Griscik, R.W. Rousseau, A.S. Teja, Crystallization of n-octacosane by the rapid expansion of supercritical solutions, J. Cryst. Growth 155 (1995) 112–119, https://doi.org/10.1016/0022-0248(95)00197-2.

[29] L. Koen, The micronisation of synthetic waxes, Master's dissertation, University of Stellenbosch, 2003.

[30] A.R. Sampaio de Sousa, A.L. Simplício, H.C. de Sousa, C.M.M. Duarte, Preparation of glyceryl monostearate-based particles by PGSS®-application to caffeine, J. Supercrit. Fluids 43 (2007) 120–125, https://doi.org/10.1016/j.supflu.2007.03.015.

[31] H.H. Franken, J.H. Knoetze, C.E. Schwarz, Concurrent measurement of high-pressure binary phase equilibrium, density and dynamic viscosity, J. Supercrit. Fluids 133 (2018) 444–454, https://doi.org/10.1016/j.supflu.2017.11.008.

[32] H.H. Franken, J.H. Knoetze, C.E. Schwarz, High-pressure binary phase equilibria, density and dynamic viscosity of 100 & 200 cSt polydimethylsiloxane (PDMS) with supercritical CO_2, J. Supercrit. Fluids 139 (2018) 1–7, https://doi.org/10.1016/J.SUPFLU.2018.04.020.

[33] N. Motang, J.H. Knoetze, C.E. Schwarz, Density and viscosity measurements at phase transition in supercritical carbon dioxide + 1-dodecanol + 2-dodecanol mixtures, J. Supercrit. Fluids 195 (2023) 105864, https://doi.org/10.1016/J.SUPFLU.2023.105864.

[34] C.E. Schwarz, I. Nieuwoudt, Phase equilibrium of propane and alkanes: Part I. Experimental procedures, dotriacontane equilibrium and EOS modelling, J. Supercrit. Fluids 27 (2003) 133–144, https://doi.org/10.1016/S0896-8446(02)00232-2.

[35] G. Kravanja, Ž. Knez, M. Knez Hrnčič, Density, interfacial tension, and viscosity of polyethylene glycol 6000 and supercritical CO_2, J. Supercrit. Fluids 139 (2018) 72–79, https://doi.org/10.1016/j.supflu.2018.05.012.

[36] D. Gourgouillon, H.M.N.T. Avelino, J.M.N.A. Fareleira, M. Nunes da Ponte, Simultaneous viscosity and density measurement of supercritical CO_2-saturated PEG 400, J. Supercrit. Fluids 13 (1998) 177–185, https://doi.org/10.1016/S0896-8446(98)00050-3.

[37] H.M.N.T. Avelino, J.M.N.A. Fareleira, D. Gourgouillon, J.M. Igreja, M. Nunes da Ponte, Viscosity of poly(ethyleneglycol) 200 [PEG 200] saturated with supercritical carbon dioxide, J. Supercrit. Fluids 128 (2017) 300–307, https://doi.org/10.1016/j.supflu.2017.02.024.

[38] B. Calvignac, E. Rodier, J.-J. Letourneau, P.M.A. dos Santos, J. Fages, Cocoa butter saturated with supercritical carbon dioxide: measurements and modelling of solubility, volumetric expansion, density and viscosity, Int. J. Chem. React. Eng. 8 (2010), https://doi.org/10.2202/1542-6580.2191.

[39] V. Bürk, M. Meinecke, S. Pollak, A. Kilzer, High-pressure density measurements of poly(ethylene glycol) 600 [PEG600] saturated with carbon dioxide with an oscillating device of advanced accuracy, J. Supercrit. Fluids 181 (2022) 105497, https://doi.org/10.1016/J.SUPFLU.2021.105497.

[40] R. Span, W. Wagner, A new equation of state for carbon dioxide covering the fluid region from the triple-point temperature to 1100 K at Pressures up to 800 MPa, J. Phys. Chem. Ref. Data 25 (1996) 1509–1596, https://doi.org/10.1063/1.555991.

[41] A.F. Collings, E. McLaughlin, Torsional crystal technique for the measurement of viscosities of liquids at high pressure, Trans. Faraday Soc. 67 (1971) 340–352, https://doi.org/10.1039/TF9716700340.

[42] Joint Committee for Guides in Metrology, Evaluation of measurement data – Guide to the expression of uncertainty in measurement, JCGM 100:2008. ⟨http://www.iso.org/sites/JCGM/GUM/JCGM100/C045315e-html/C045315e.html⟩.

[43] J. Doucet, I. Denicolo, A. Craievich, X-ray study of the "'rotator"' phase of the odd-numbered paraffins $C_{17}H_{36}$, $C_{19}H_{40}$, and $C_{21}H_{44}$, J. Chem. Phys. 75 (1981) 1523–1529, https://doi.org/10.1063/1.442185.

[44] J. Doucet, I. Denicolo, A. Craievich, A. Collet, Evidence of a phase transition in the rotator phase of the odd-numbered paraffins $C_{23}H_{48}$ and $C_{25}H_{52}$, J. Chem. Phys. 75 (1981) 5125–5127, https://doi.org/10.1063/1.441904.

[45] S.P. Srivastava, J. Handoo, K.M. Agrawal, G.C. Joshi, Phase-transition studies in n-alkanes and petroleum-related waxes—a review, J. Phys. Chem. Solids 54 (1993) 639–670, https://doi.org/10.1016/0022-3697(93)90126-C.

[46] W.R. Turner, Normal Alkanes, Ind. Eng. Chem. Prod. Res. Dev. 10 (1971) 238–260. ⟨https://pubs.acs.org/doi/pdf/10.1021/i360039a003⟩.

[47] V. Trivedi, R. Bhomia, J.C. Mitchell, N.J. Coleman, D. Douroumis, M.J. Snowden, Study of the effect of pressure on melting behaviour of saturated fatty acids in liquid or supercritical carbon dioxide, J. Chem. Eng. Data 58 (2013) 1861–1866, https://doi.org/10.1021/je400260c.

[48] R. Bhomia, V. Trivedi, J.C. Mitchell, N.J. Coleman, M.J. Snowden, Effect of pressure on the melting point of pluronics in pressurised carbon dioxide, Ind. Eng. Chem. Res. 53 (2014) 10820–10825, https://doi.org/10.1021/ie501344m.

[49] E. Kukova, M. Petermann, E. Weidner, Phase behaviour (S-L-G) and fluid dynamic properties of high viscous polyethylene glycols in the presence of compressed carbon dioxide, Proc. 6th ISSF (2003) 1547–1552.

[50] P.W. Labuschagne, B. Naicker, L. Kalombo, Micronisation, characterisation and in-vitro dissolution of shellac from PGSS supercritical CO_2 technique, Int. J. Pharm. 499 (2016) 205–216, https://doi.org/10.1016/j.ijpharm.2015.12.021.

[51] M. Yasuniwa, C. Nakafuku, High pressure crystallisation of ultra-high molecular weight polyethylene, Polym. J. 19 (1987) 805–813, https://doi.org/10.1295/polymj.19.805.

[52] J. Le Roux, N. Loubser, Nuclear magnetic resonance investigation of the mobile phase in paraffinic Fischer-Tropsch waxes, S. Afr. J. Sci. 76 (1980) 157–161. ⟨https://journals.co.za/doi/pdf/10.10520/AJA00382353_1815⟩.

[53] J.A.J. Lourens, E.C. Reynhardt, NMR investigation of Fischer-Tropsch waxes, J. Phys. D. Appl. Phys. 12 (1979) 1963, https://doi.org/10.1088/0022-3727/12/11/024.

[54] J.J. Retief, J.H. Le Roux, Crystallographic investigations of a paraffinic Fischer-Tropsch wax in relation to a theory of wax structure and behaviour, S. Afr. J. Sci. 79 (1983) 234–239. ⟨https://journals.co.za/doi/pdf/10.10520/AJA00382353_2317⟩.

[55] E C Reynhardt, NMR investigation of Fischer-Tropsch waxes. II. Hard wax, J. Phys. D. Appl. Phys. 18 (1985) 1185, https://doi.org/10.1088/0022-3727/18/6/021.

[56] I. Basson, E.C. Reynhardt, The structure and melting of paraffinic Fischer—Tropsch waxes, Chem. Phys. Lett. 198 (1992) 367–372, https://doi.org/10.1016/0009-2614(92)85066-J.

[57] I. Basson, E.C. Reynhardt, Defect chain motions in the low temperature phase of multiple mixtures of n-alkanes by means of nuclear magnetic resonance spin–lattice relaxation time measurements, J. Chem. Phys. 97 (1992) 1287–1295, https://doi.org/10.1063/1.463255.

[58] D.L. Dorset, Bridged Lamellae: Crystal Structure(s) of Low Molecular Weight Linear Polyethylene, Macromolecules 32 (1999) 162–166, https://doi.org/10.1021/ma981371r.

[59] D.L. Dorset, The bridged lamellar structure of synthetic waxes determined by electron crystallographic analysis, J. Phys. Chem. B 104 (2000) 4613–4617, https://doi.org/10.1021/jp994380q.
[60] C.E. Schwarz, High pressure phase behaviour of the homologous series CO_2 + 1 -alcohols, J. Chem. Eng. Data 63 (2018) 2451–2466, https://doi.org/10.1021/acs.jced.7b01000.
[61] P. Ilieva, A. Kilzer, E. Weidner, Measurement of solubility, viscosity, density and interfacial tension of the systems tristearin and CO_2 and rapeseed oil and CO_2, J. Supercrit. Fluids 117 (2016) 40–49, https://doi.org/10.1016/j.supflu.2016.07.014.
[62] A.R.S. de Sousa, M. Calderone, E. Rodier, J. Fages, C.M.M. Duarte, Solubility of carbon dioxide in three lipid-based biocarriers, J. Supercrit. Fluids 39 (2006) 13–19, https://doi.org/10.1016/j.supflu.2006.01.014.
[63] P. Münüklü, F. Wubbolts, T.W. De Loos, P.J. Jansens, The phase behaviour of systems of supercritical CO_2 or propane with edible fats and a wax, J. Supercrit. Fluids 39 (2006) 1–5, https://doi.org/10.1016/J.SUPFLU.2006.01.011.
[64] S.P. Srivastava, J. Handoo, K.M. Agrawal, G.C. Joshi, Phase-transition studies in n-alkanes and petroleum-related waxes—a review, J. Phys. Chem. Solids 54 (1993) 639–670, https://doi.org/10.1016/0022-3697(93)90126-C.
[65] E. Jenab, F. Temelli, Viscosity measurement and modelling of canola oil and its blend with canola stearin in equilibrium with high pressure carbon dioxide, J. Supercrit. Fluids 58 (2011) 7–14, https://doi.org/10.1016/j.supflu.2011.05.001.
[66] T. Fornari, E.J. Hernández, G. Reglero, Solubility of supercritical gases in organic liquids, J. Supercrit. Fluids 51 (2009) 115–122, https://doi.org/10.1016/J.SUPFLU.2009.08.015.
[67] J. Méndez-Santiago, A.S. Teja, The solubility of solids in supercritical fluids, Fluid Phase Equilib. 158–160 (1999) 501–510, https://doi.org/10.1016/S0378-3812(99)00154-5.
[68] J. Chrastil, Solubility of solids and liquids in supercritical gases, J. Phys. Chem. 86 (1982) 3016–3021, https://doi.org/10.1021/j100212a041.
[69] E. Hernandez, G. Reglero, T. Fornari, Correlating the solubility of supercritical gases in high-molecular weight substances using a density-dependent equation, AIChE J. 57 (2011) 765–771, https://doi.org/10.1002/aic.12283.
[70] R.C. Narayan, J.V. Dev, G. Madras, Experimental determination and theoretical correlation for the solubilities of dicarboxylic acid esters in supercritical carbon dioxide, J. Supercrit. Fluids 101 (2015) 87–94, https://doi.org/10.1016/J.SUPFLU.2015.03.008.
[71] C.E. Schwarz, High Pressure phase equilibria of the CO_2/saturated ethyl esters homologous series, J. Chem. Eng. Data 63 (2018) 1006–1020, https://doi.org/10.1021/acs.jced.7b00780.